Climate Dynamics
https://doi.org/10.1007/s00382-018-4466-y

The anomalous 2017 coastal El Niño event in Peru

C. Rodríguez-Morata[1] · H. F. Díaz[2] · J. A. Ballesteros-Canovas[1,3] · M. Rohrer[1,4] · M. Stoffel[1,3,5]

Received: 20 March 2018 / Accepted: 22 September 2018

Abstract

Remarkably heavy and devastating rainfalls affected large parts of Peru during the austral summer 2016–2017. These rainfalls favoured widespread land sliding and extensive flooding and generated one of the most severe disasters of Peru since the 1997–1998 El Niño event. The amount of rainfall recorded between January and March 2017 only compares to the biggest El Niño events of the last 40 years (i.e. 1982–1983 and 1997–1998) and exceeded the 90th percentile of available records (1981–2017) over much of the northern and central coasts of Peru, the Andean region and Amazonia. The occurrence of these heavy rainfalls was highly anomalous as it occurred during the first austral summer following the development and decay of a very strong El Niño in 2015–2016. Here, we propose that the likely cause of the anomalous rainfalls is linked to the combination of an especially intense wet spell over the Central Andes related to a deep, long-lasting anticyclone located adjacent to the Chilean coast, and to the unusual development of warm water off the coast of Peru in the nominal El Niño 1 + 2 region. This warming has been related to an anomalous weakening of the mid-upper level subtropical westerly flow, which in turn led to a weakening of the southeasterly trades off the coast, thus hindering the upwelling near the Peruvian coast and favoring the eastern Pacific warming. This development is counter to the usual evolution of sea surface temperature in the eastern equatorial Pacific following very strong El Niño events, such as those occurred in 1982–1983, 1997–1998, and 2015–2016. This paper explores the unusual nature of this event in the observational record and illustrates its consequences.

Keywords Coastal El Niño · Sea surface temperature · Rainfalls · Flooding · Peru

1 Introduction

During the 2016–2017 austral summer, Peru experienced widespread and unusually heavy rainfall, which triggered landslides and severe flooding, thereby leading to catastrophic damage to housing and infrastructure, and affecting more than 6,60,000 people, and leaving more than 100 deaths (INDECI 2017). The areas most affected by the disaster were located in the northern and central coastal regions of Peru (Fig. 1), as well as southeast of the Loreto region in the Peruvian Amazonas basin. In addition to the death tolls and physical injuries, these heavy rainfalls also resulted in increased exposure of local populations to disease pathogens and mental health problems associated with loss, disruption, and displacement (Hales et al. 2003; Waring and Brown 2005; Few 2007). In the context of the 2016–2017 extreme rainfall season 6270 dengue cases were confirmed in Peru (PAHO 2017), which triggered the declaration of a sanitary emergency by the Ministry of Health (MINSA) in seven regions of Peru. The heavy rainfalls of the 2016–2017 austral summer were highly anomalous because they occurred

Electronic supplementary material The online version of this article (https://doi.org/10.1007/s00382-018-4466-y) contains supplementary material, which is available to authorized users.

✉ C. Rodríguez-Morata
Clara.Rodriguez@unige.ch

1 Climate Change Impacts and Risks in the Anthropocene (C-CIA), Institute for Environmental Sciences, University of Geneva, Boulevard Carl-Vogt 66, 1205 Geneva, Switzerland

2 Department of Geography and Environment, University of Hawai'i at Manoa, Honolulu, USA

3 Dendrolab.ch, Department of Earth Sciences, University of Geneva, Rue des Maraîchers 13, 1205 Geneva, Switzerland

4 Meteodat GmbH, Technoparkstrasse 1, 8005 Zurich, Switzerland

5 Department F.A. Forel for Aquatic and Environmental Sciences, University of Geneva, Boulevard Carl-Vogt 66, 1205 Geneva, Switzerland

Published online: 27 September 2018

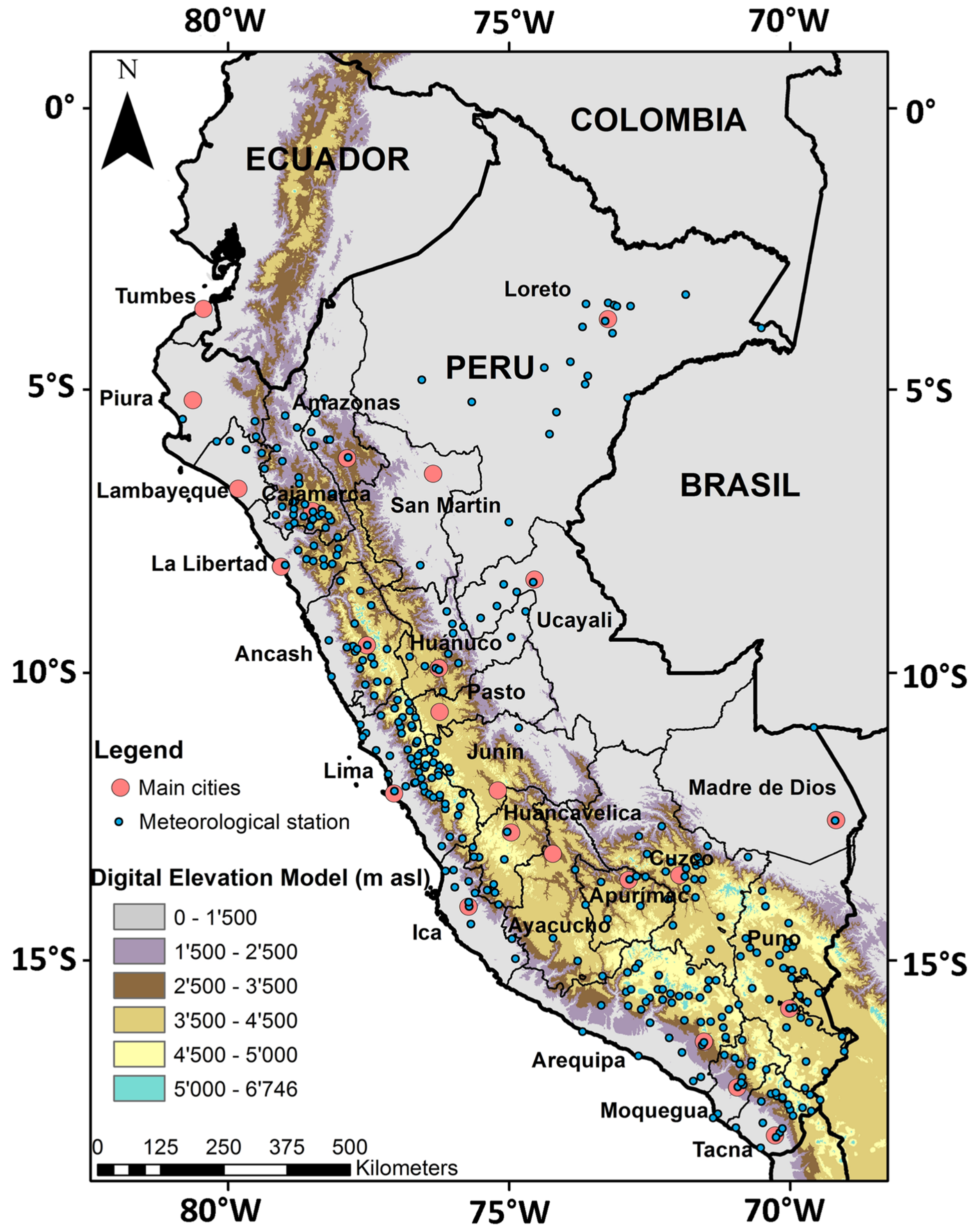

Fig. 1 Geographical distribution of regions and rain gauges used in this study. A digital elevation model shows the topographical characteristics and altitudes of Peru

during the first austral summer following the development and decay of a very strong El Niño in 2015–2016. The rainfall recorded between January and March 2017 exceeded the 90th percentile of available measurements for the period 1981–2017 over much of the northern and central coasts of Peru, the Andean region and Amazonia. This event is only comparable to the rainfall measured during the largest El Niño events of the last 40 years (i.e. 1982–1983 and 1997–1998). Interestingly, in these areas, rainfall totals during the 2016–2017 austral summer exceeded those recorded during the 2015–2016 El Niño event. The 2015–2016 El Niño has been classified as a strong event by the international community, even if it has had much less dramatic consequences for Peru than the strong El Niño events in 1972–1973, 1982–1983, and 1997–1998 (L'Heureux et al. 2017; Sanabria et al. 2018).

Rainfall during the 2016–2017 austral summer occurred in conjunction with largely negative (positive) SST anomalies in the central (eastern) equatorial Pacific off the coast of South America. Based on the monthly "ENSO Diagnostic Discussion Archive" from the Climate Prediction Center (CPC 2018a), below normal SST anomalies were registered in the Niño 3.4 region for November and December 2016, suggesting a developing La Niña event (NOAA 2017). The Oceanic Niño Index (ONI) however extends La Niña status from July–September 2016 to November-January 2017 (CPC 2018b). However, during January 2017 and extending through March 2017, a strong positive SST anomaly was observed in the 1 + 2 region, leading to an event which has previously been referred to a "Coastal El Niño" (Takahashi and Martínez 2017; hereafter CEN-2017). Therefore, a watch status was put in place at the end of January 2017, and an alert status was issued between February and May 2017 (ENFEN 2017a, b).

The observed SST anomaly event in the equatorial Pacific during the 2016–2017 austral summer was highly atypical because it occurred during the austral summer season, and at a time when the 2015–2016 El Niño event was in its last phase of decay (L´Heureux et al. 2017). The situation in early 2017 differed substantially from previous summers following strong El Niños in terms of the spatio-temporal SST pattern. Thus, the 2016–2017 rainfall event cannot be classified with classical ENSO definitions (i.e. Rasmusson and Carpenter 1982; Ashok et al. 2007; Kug et al. 2009; Yeh et al. 2009; Kao and Yu 2009; Takahashi et al. 2011; Yu et al. 2011). The reasons for this may be related to the fact that (1) the 2016–2017 austral summer event was not a clearly coupled ocean–atmosphere phenomenon in the equatorial Pacific (Garreaud 2018), and that (2) the warming was not present throughout the Equatorial Pacific Basin.

The ENSO cycle may present strong variability in terms of its amplitude, temporal evolution, and spatial pattern (Larkin and Harrison 2005; Ashok et al. 2007; Takahashi et al. 2011; Dommenget et al. 2013; Capotondi et al. 2015). For instance, Takahashi and Martinez (2017) describe a previous coastal event in 1925 as the result of cold conditions in the western-central equatorial Pacific that would have helped to destabilize the ITCZ and generate strong northerly winds across the equator. More recently, Garreaud (2018) developed a first approximation to the origin of the CEN-2017 providing a reasonable description of the atmospheric forcing involved in the origin of the coastal SST overwarming. This author proposed that during the recent coastal El Niño, an external forcing provided by vacillations in the free-tropospheric subtropical westerlies would have led to a weakening of the SE trades at lower levels and consequently to the increase of coastal SST.

In this paper, we take advantage of the information contained in these previous works to extend our understanding about (1) the atmospheric and oceanic context during the 2016–2017 austral summer in Peru, and (2) the impacts it has had on the magnitude, distribution, and timing of extreme rainfalls that occurred over Peru. To this end, we first describe the CEN-2017 event and related impacts in Peru before we explore how different this event was compared to others in the historical record. We use different reanalysis data for SST and atmospheric variables as well as gridded and observational rainfall data sources to contextualize the 2016–2017 austral summer precipitation and to describe the spatio-temporal evolution of the event during this period.

2 Data and methods

2.1 Precipitation analysis

We used rainfall information from 338 Peruvian gauge stations, provided by the National Service of Meteorology and Hydrology of Peru (SENAMHI), the MeteoDat portal (Schwarb et al. 2011) as well as gridded data from the GPM IMERG dataset (Huffman 2015) to characterize the spatial distribution and intensity of accumulated rainfall during the 2016–2017 DJFM austral summer. Gauge stations are distributed all along the country but major density is founded in the most populated coastal regions (Fig. 1). Yet, rainfall records of these stations are not always continuous and the number of gauge stations with a full record for each month can vary substantially. Gridded satellite data from GPM IMERG has a spatial resolution of $0.1° \times 0.1°$ but only covers the period between 2014 to the present (extended information is available at https://pmm.nasa.gov/index.php?q=GPM). In fact, it is possible that observed values from gauge stations can be different from GPM Imerg values for the same location. This is due to (1) the inherent error associated with the precipitation model (Huffman et al. 2017) and (2) the $0.1° \times 0.1°$ spatial resolution of the GPM data, meaning that rainfall values are in fact average values of an area of 121 km^2 for which differences in precipitation must be expected at more local scales.

To provide further context for the magnitude of the precipitation event, we have used gridded data ($1° \times 1°$) from GPCC Monitoring Product (Schneider et al. 2015) as well as observational data from 73 Peruvian gauge stations covering the entire period (1982–2017), (i.e. 17 gauge stations for the month of December; 40 for January; 24 for February and 34 for March). With this data base, we have computed rank percentile maps of precipitation to compare the 2016–2017 DJFM monthly precipitation with rainfall data for the same period over the last 36 years (1982–2017).

2.2 Large-scale atmospheric and oceanic synoptic analysis of the 2016–2017 coastal event

The domain of the synoptic analyses covers the entire South American continent and part of the East Pacific and West Atlantic oceans and is large enough to capture the main features of climate variability over South America [i.e., the Bolivian High (BH), the South American monsoon (SAH), Intertropical Convergence Zone (ITCZ), and the South Atlantic Convergence Zone (SACZ); Garreaud et al. 2009]. At high levels (i.e., 200 hPa), the Bolivian High (BH) is the major synoptic feature occurring during austral summers (Lenters and Cook 1997). It consists in a closed anticyclone developing over the central Andes, which forms in response to latent heat released during deep convection over the Amazon basin (Sulca et al. 2016).To describe the CEN-2017, we have used daily data of geopotential height, wind velocity components, outgoing longwave radiation (OLR) and sea surface temperature (SST) from the NCEP/NCAR reanalysis (Kalnay et al. 1996) and provided by the NOAA/OAR/ESRL PSD (http://www.esrl.noaa.gov/psd/). This data is available on a 2.5° × 2.5° grid at 17 pressure levels. Anomalies refer to the 1981–2010 climatology. Outgoing long-wave radiation (OLR) anomalies were used as a proxy for convective processes (NCAR 2014). Negative (positive) OLR anomalies are indicative of enhanced (suppressed) convection and hence more (less) cloud coverage. More (less) convective activity in the central and eastern equatorial Pacific implies higher (lower), colder (warmer) cloud tops, which emit much less (more) infrared radiation into space.

Analysis of the dominance and changes of synoptic patterns over time between December 2016 and March 2017 (at the daily scale) was performed with Self Organizing Maps (SOMs; Kohonen 2001; Hewitson and Crane 2002; Reusch et al. 2005a, b, 2007; Cassano et al. 2006a). To this end, we have used geopotential and zonal wind anomalies at 200, 500, and 850 hPa as well as daily SST data, with a spatial resolution of 2.5° × 2.5°, from the ERA-Interim reanalysis climate data set (ECMWF 2016) with a time span from 1979 to present (Dee et al. 2011). ERA-Interim data was retrieved from http://www.ecmwf.int/research/era.

2.2.1 Self-organizing maps

Self-organizing maps (SOM) represent a clustering technique that allows summarizing large, high-dimensional records by treating data as a continuum. SOM identify patterns using an iterative clustering algorithm (Hewitson and Crane 2002), and produce a set of nodes (i.e., generic synoptic states directly interpretable as physical process states) in a two-dimensional lattice with similar states close to each other and the most extreme states at the opposite corners. Analyses of these nodes allow the characterization of the frequency of each synoptic state, the spatio-temporal transitions between states as well as their dominance in a given temporal horizon (Kohonen 2001; Hewitson and Crane 2002).

This technique has been used successfully in many meteorological, climatological, and oceanic research applications worldwide, either to characterize extreme weather and rainfall events (Hong et al. 2005; Cassano et al. 2006a, b; Morata et al. 2006; Zhang et al. 2006; Uotila et al. 2007; Schuenemann et al. 2009), including in the Peruvian Amazon and Andes regions (Espinoza et al. 2012, 2013; Paccini et al. 2017; Rodriguez-Morata et al. 2018), to visualize synoptic weather patterns over a region (Hewitson and Crane 2002; Reusch et al. 2005a, b, 2007; Johnson et al. 2008; Seefeldt and Cassano 2008; Wise and Dannenberg 2014), or to evaluate Global Climate Model (GCM) results (Lynch et al. 2006; Cassano et al. 2007; Skific et al. 2009a, b).

Initially, SOMs are formed by an arbitrary number of clusters or nodes. Each cluster is associated with two vectors. The first vector describes the position of the cluster on the lattice, whereas the second (also referred to as reference vector) represents the position of the cluster centroid in the data space. By using an iterative process, an unsupervised algorithm is applied to adjust the reference vectors representing the nodes based on the differences between the reference vectors and each input value. In each iteration, the Euclidean distance between input data and reference vectors is calculated and the best matching reference vector is identified for each input record. Neighboring reference vectors of each best match are then updated to result in adjacent nodes having the strongest similarity. Iterations are ended when stable values of the reference vectors are reached. The choice of the number of nodes depends on the specific research context and amount of data. Generally, smaller (larger) number of nodes implies less (more) possibilities to characterize the high-dimensional data space and therefore more (less) generalization of the input data.

To analyze the 2016–2017 austral summer event, we defined a 5 × 5 nodes lattice to best discriminate the main synoptic South American summertime features including those patterns associated with ENSO (positive and negative phases). The SOM analysis was carried out with the MeteoLab toolbox for Matlab (http://grupos.unican.es/ai/meteo/MeteoLab.html) using a linear decay to zero for both the learning rate and neighborhood amplitude after 5000 cycles. Input records (i.e. days) with common synoptic patterns were then linked to the same SOM node or cluster. The resulting set of clusters (SOM) represents meaningful subgroups (i.e. generic climatic patterns) within the larger dataset. To identify these groups (i.e. nodes) we used a coordinate system naming the rows with numbers (i.e. 1–5) and the columns with letters (i.e. A–E). Note that while several variables can be jointly analyzed only one SOM grid is produced and each SOM node contains the four variables. However, for clarity, SOM maps for each variable are shown separately. The daily scale of our study has allowed us to construct frequency maps of the SOM grid for each austral summer (DJFM) since 1979, thereby allowing us to track transitions between synoptic states and the dominance (i.e. the number of days that a synoptic pattern is present during the austral summer) of each state.

2.3 Interannual comparison of austral summers

We have used the OLR anomaly of the NOAA/Monthly Mean upward longwave flux at top of the atmosphere dataset since 1979 (http://climexp.knmi.nl/select.cgi?field=umd_olr) as well as SSTs from the HadISST1 data set, and derived El Niño 1 + 2 and 3.4 indices (Rayner et al. 2003) to assess similarities/differences between the 2016–2017 rainfall event and other austral summers since 1870. HadISST1 has a monthly resolution, from 1870 to date, and is available on a 1° × 1° grid. The use of the 3.4 and 1 + 2 SST indices served to separate the different behavior in the central (3.4; 5°N–5°S, 170°W–120°W) and eastern (1 + 2; 0°–10°S, 90°W–80°W) Pacific, since SST in these two regions modulate rainfall over Peru in different ways (Lavado-Casimiro and Espinoza 2014; Sulca et al. 2017). Indices were obtained from https://www.esrl.noaa.gov/psd/gcos_wgsp/Timeseries/. We employed a Superposed Epoch Analysis (SEA) to compare 1 + 2 and 3.4 El Niño indices based on SST standardized monthly anomalies corresponding to all summers after El Niño events since 1950 (this is the temporal limitation of the ONI index). The selection of El Niño events was based on the classification of the Oceanic Niño Index (ONI) (http://www.cpc.noaa.gov/products/analysis_monitoring/ensostuff/ensoyears.shtml). This index is most commonly used to define El Niño and La Niña events and is based on SST anomalies in the Niño 3.4 region, which represents the average equatorial SSTs across the Pacific from about the dateline to the South American coast (Trenberth 2016). The ONI uses a 3-month running mean, and to be classified as a full-fledged El Niño or La Niña, the anomalies must exceed + 0.5 °C or − 0.5 °C for at least five consecutive months. Furthermore, we wanted to compare the SST distribution in the equatorial Pacific during the CEN-2017 event with its counterpart post-strong El Niño austral summers in 1878–1879, 1983–1984 and 1998–1999. Statistical analyses have been carried out using the t-test for one-sided sample (Haynes 2013) at significance level of 0.05.

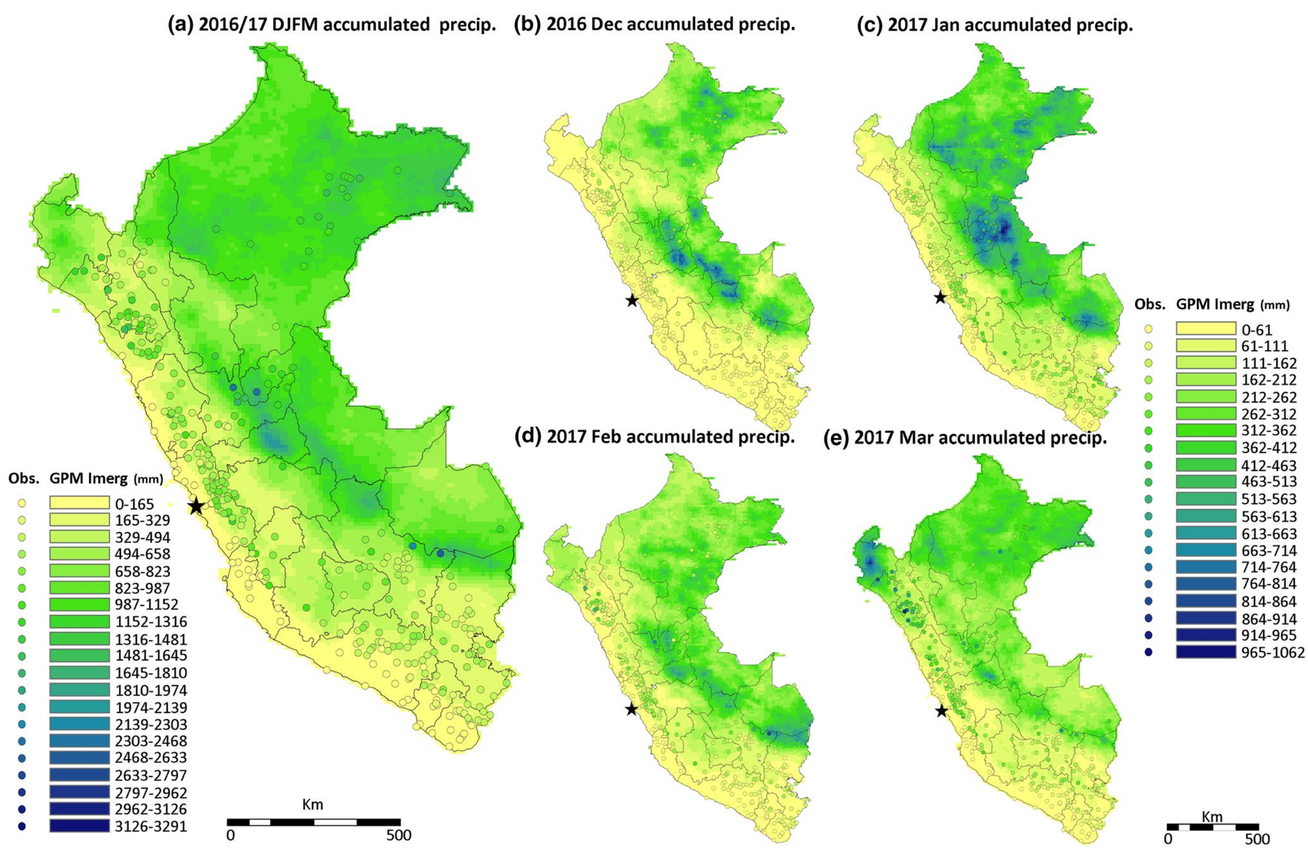

Fig. 2 Maps representing the DJFM 2016–2017 accumulated rainfall using data from (1) 300 rain gauges distributed all along Peru and (2) GPM IMERG gridded data of 0.1° × 0.1° spatial resolution. Black star is indicating the location of Lima. Note that the scale range is different for the accumulated rainfall for the entire period from DJFM (**a**) and at monthly scale (**b**–**e**)

3 Results

3.1 December–March precipitation analysis over Peru

From December 2016 to February 2017, accumulated precipitation over Peru (Fig. 2) varied from extremely low values (Obs.: 0 mm; GPM: 31.76 mm; Fig. 2a) to unusually high totals (Obs.: 3291 mm; GPM: 2142 mm; Fig. 2a). By month, data from stations indicate that the highest values of rainfall were recorded in March (1062 mm; Fig. 2e) in the station of Pasaje Sur, in the north of Lambayeque region. December 2016 (Fig. 2b) exhibits the second highest value (856.2 mm) in El Boquerón station, in the border between the Huánuco and Ucayali regions. January 2017 (Fig. 2c) recorded its maximum at the same station (812.1 mm) and February 2017 rainfalls (Fig. 2d) were highest at Quincemil station (831.1 mm) located at the border between Cuzco and Madre de Dios.

Rank percentile maps (Fig. 3) show that many areas of Peru received cumulative precipitation totals between

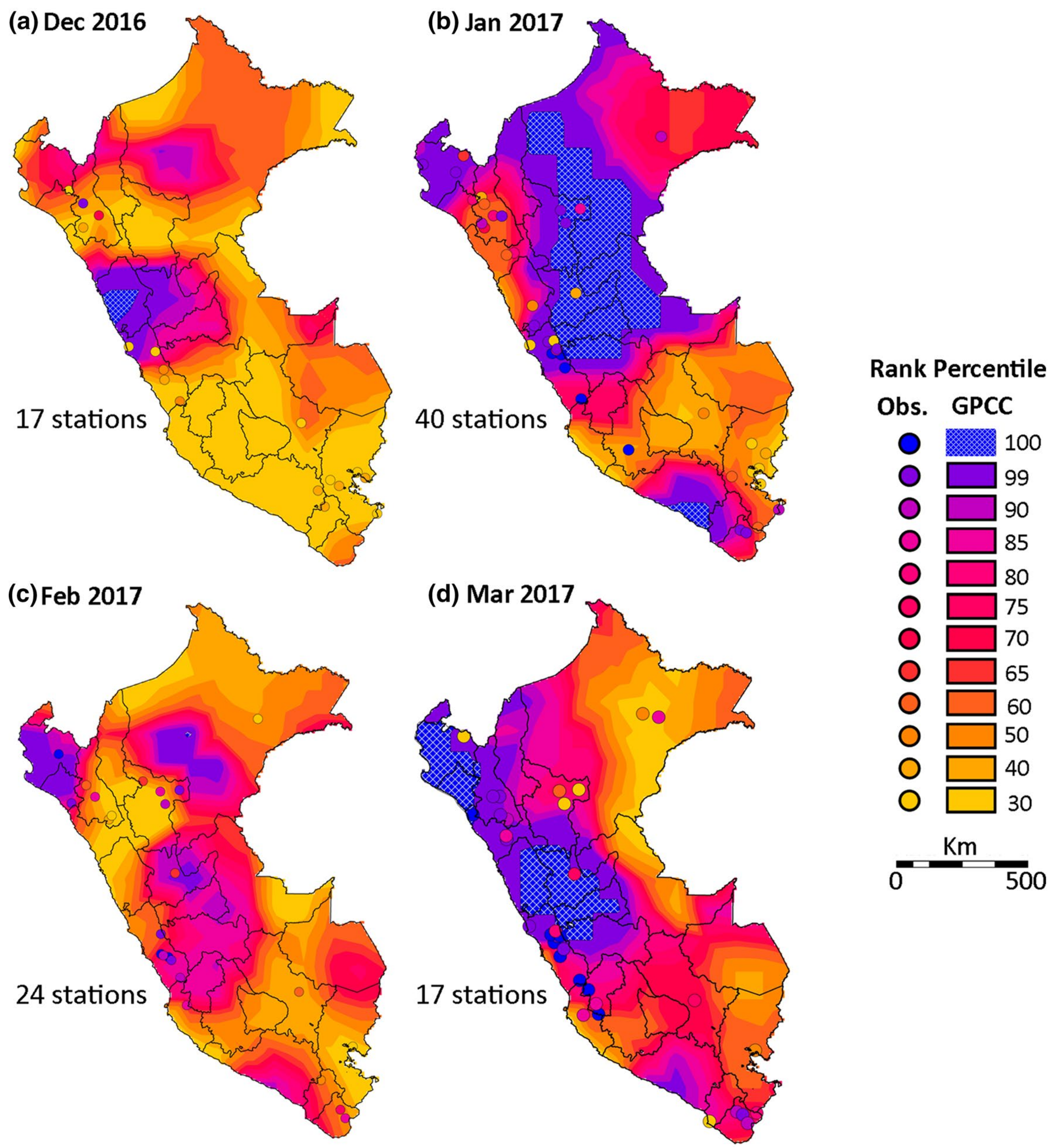

Fig. 3 Rank percentile maps for DJFM 2016–2017. The number of stations available for each month varies substantially. We indicate the number of stations having a full record for the period 1982–2017 for each month

December 2016 and March 2017 that exceed all values recorded since 1982. Regarding GPCC data by month, cumulative precipitation exceeded the 80th percentile in only some parts (7.9%) of the country in December 2016 (Fig. 3a). In west Loreto and in the Ancash region precipitation totals were over the 90th percentile or even unprecedented (i.e. 100th) in the case of the Ancash coast. By contrast, in the other parts of Peru, rainfall totals remained under the 50th percentile. During January 2017 (Fig. 3b), the 80th percentile was exceeded in 35.8% of the country, whereas the 90th percentile was exceeded along the North (i.e. Tumbes and Piura) and Central coast (i.e. Ancash and Lima). Unprecedented values were seen along the South coast (i.e. Arequipa), Central Andes (i.e. San Martin, Huánuco, Pasto and Junín) as well as in the Amazonian lowlands (i.e. south-west Loreto, Amazonas and Ucayali). In February 2017 (Fig. 3c), cumulative precipitation exceeded the 80th percentile over 17% of the country but values above the 90th percentile were still observed along the North coast (i.e. Piura and Lambayeque) as well as west of the Loreto and Huánuco regions. During March 2017 (Fig. 3d), more than one-fourth of the country (28.5%) shows percentile values above the 80th percentile and two spots – i.e. along the North coast (Tumbes and Piura) and in the Central Andes (Huánuco, Pasto, Junin and Ancash) exhibit 100th percentile values.

From the 17 gauge station records available for December 2016, only two show rank percentiles above the 60th percentile: Bambamarc (66th) and Querocotillo (97th). In line with the GPCC data, the other stations present values under the 50th percentile. In January 2017, out of 40 stations, 25 exhibit values above the 60th, 15 above the 90th and 5 reached the 100th percentile, most of the latter being located in the western part of the Peruvian Central Andes. From the 24 stations available for February 2017, 17 exhibited values above the 60th, 7 above the 90th and 3 reached the 100th percentile, again on the western Andean slopes but also along the north coast of Peru. In March 2017 (for which 34 stations are available), 27 stations show values above the 60th, 16 above the 90th and 8 reaching the 100th percentile, all of the latter are located along the west Andean slope.

3.2 Large-scale atmospheric and oceanic synoptic analysis of the 2016–2017 coastal event

3.2.1 Event description

From December 2016 to March 2017, consecutive geopotential anomalies at 200 hPa occur adjacent to the Chilean coast centered at 33°S (Fig. 4a). The biggest anticyclonic anomaly developed on 20th January 2017 and lasted about 2 weeks with values above 112 gpm reaching positive anomalies of

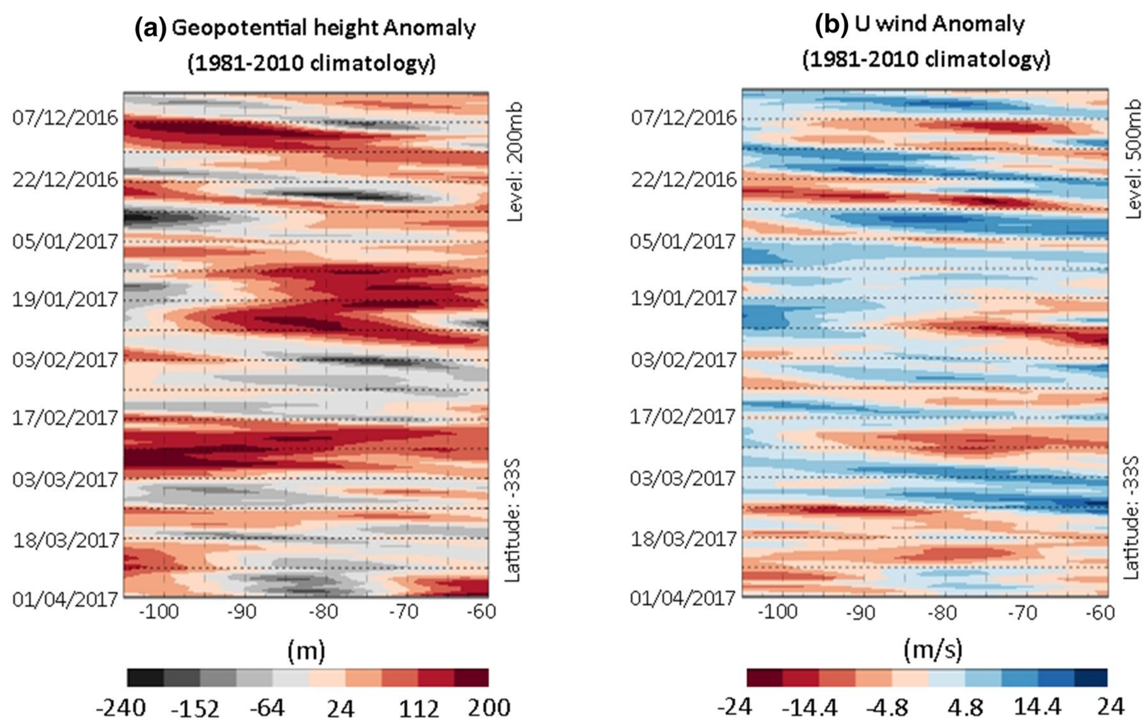

Fig. 4 Time-longitude plots for the period 1/12/2016 to 30/4/2017 averaged at latitude 33°S. **a** Geopotential height anomaly at 200 hPa. **b** Zonal wind anomaly at 500 hPa. Several periods of positive geopotential anomalies are observed and concurrent with strong negative anomalies in the zonal winds at the free troposphere (red colors in both plots)

200 gpm in some periods. Furthermore, two other, similar events occur in February and March 2017 but were of shorter duration and less intense with anomaly values ranging between 90 and 158 gpm. Coincident with these height anomalies, strong negative zonal wind anomalies are observed at 500 hPa with net velocity values ranging between 14.4 and 24 m/s (Fig. 4b). The negative character of these wind anomalies indicates a weakening of the westerly wind component and therefore a strengthening of the easterly component at 33°S. The average of the 1000 hPa vector wind anomaly along the Peruvian coast between January 20 and March 25, 2017, displays a common west-east vector wind anomaly pattern just off the north coast of Peru (Fig. 5a) with a maximum speed wind anomaly of 4.8 m/s. Figure 5b–d represent the situation corresponding with the strongest 5-day anomalies of specific events for January, February, and March, with highest speed anomalies occurring in February and March with 5.1 and 5.2 m/s, respectively, just off the north coast (Fig. 5c,d).

Large-scale convection development during the CEN-2017 event is represented by OLR anomalies in Fig. 6. In December, the main convection center is located in the Amazon basin, while a secondary area starts to develop over the south of Brazil (Fig. 6a). Later in January, in this second area an enhancement of the negative anomaly of the OLR can be seen with a net maximum value of -30 W/m^2, indicating an increase of the convective activity (Fig. 6b). Additionally, the shape of this feature extends in a NW–SE diagonal forming a band of convection typical of the South Atlantic Convergence Zone (SACZ). Also during January, negative OLR anomalies increase along the Peruvian and north Chilean coast. In February, the convective band associated with the SACZ is less intense (higher values of OLR) and moves southward. At the same time an intense convective band progress in the central-east equatorial Pacific (Fig. 6c). During March, the anomaly associated with the SACZ practically disappears and the most extensive convective center is located in the eastern equatorial Pacific adjacent to the northern Peruvian coast with negative OLR anomalies of 30 W/m^2 (Fig. 6d).

The spatio-temporal propagation of the absolute SST in the equatorial Pacific as well as along the Peruvian coast from November 2016 to November 2017 is represented in Fig. 7. Thus, for 0°–10°S (El Niño region 1 + 2; Fig. 7a) SST values raised abruptly by 2 °C (from 25 to 27 °C) along the Peruvian north coast around mid-January until they progressively reach SST values > 30 °C between mid-February and mid-March (Fig. 7a). On the other hand, for 10°S–17°S (Fig. 7b), SST were more moderate along the south-central coast of Peru (Fig. 7b) with maxima of 28 °C in mid-March. Considering SST anomalies (Fig. 8), December 2016 was characterized by negative SST anomalies in the central-eastern Pacific (3 and 3.4 Niño regions) and close to neutral SST prevailed in region 1 + 2 (Fig. 8a). During January 2017,

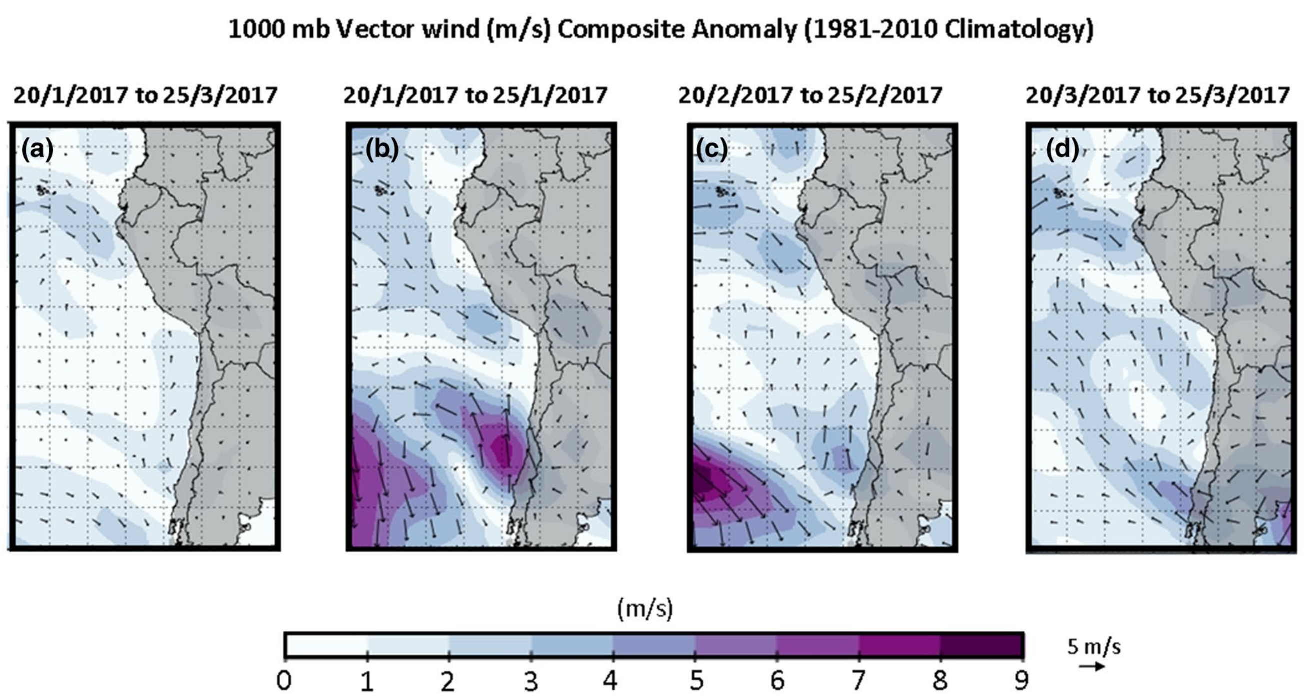

Fig. 5 Near surface vector wind anomalies between January and March 2017 indicating a trend from the west to the east in the equatorial band and along the South American coast thus indicating easterlies weakening. **a** Average anomaly from January 20th to March 25th. **b–d** the situation for different moments is concurrent with the U wind negative anomalies represented in the Fig. 4b

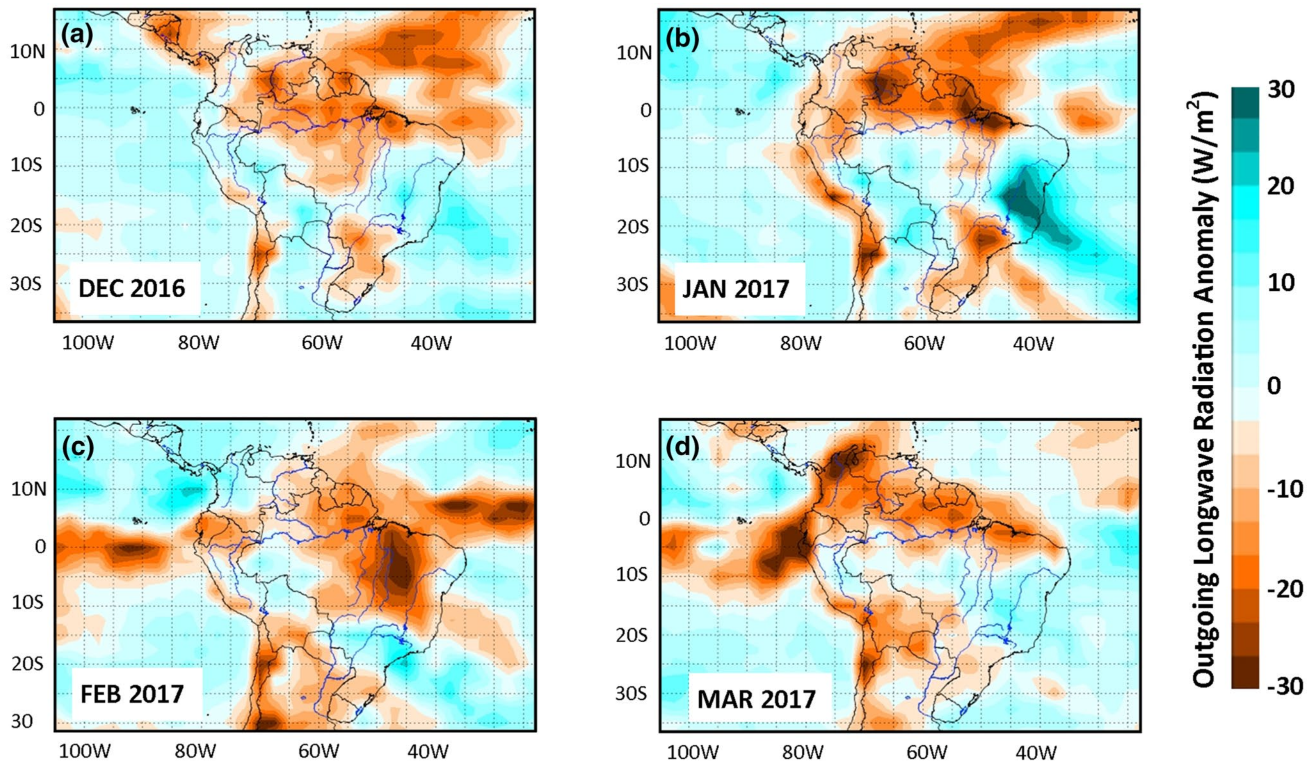

Fig. 6 Monthly Outgoing Longwave Radiation (OLR) anomaly for December 2016 to March 2017

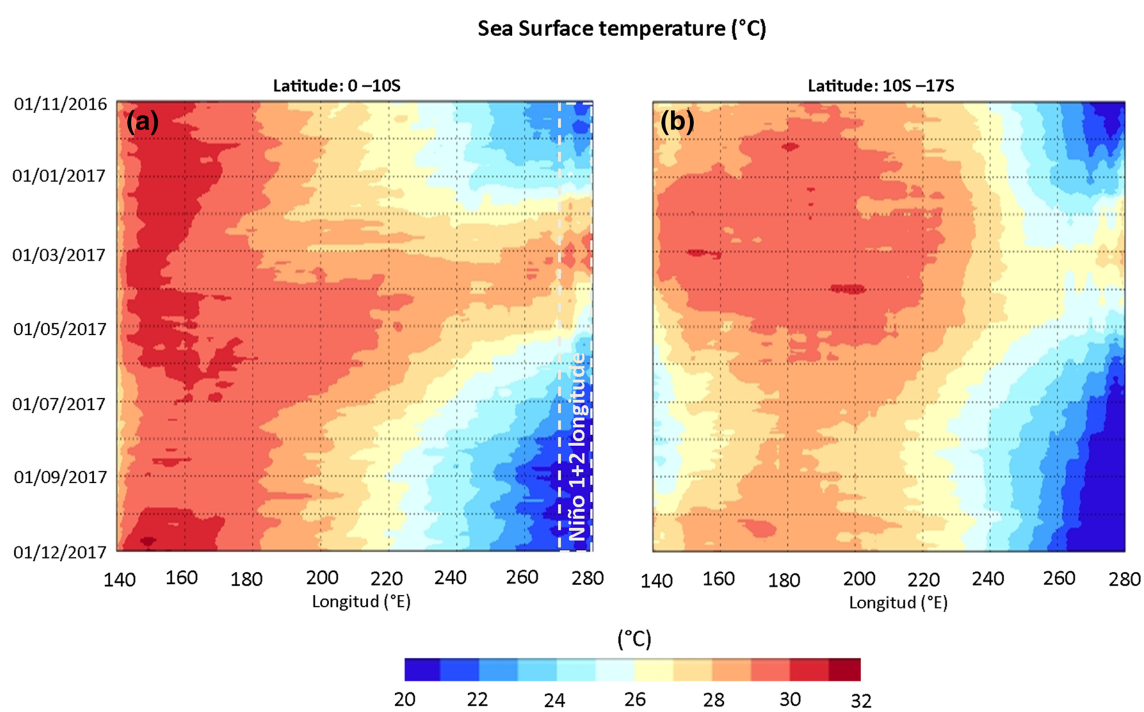

Fig. 7 Sea surface temperature (SST) time-longitude plot showing the overwarming in the South Pacific averaged to **a** El Niño 1+2 region (averaged between 0° and 10°S); and **b** along the center and south Peruvian coast (averaged between 10°S and 17°S). Data provided by the NOAA/ESRL Physical Sciences Division, Boulder Colorado from their Web site at http://www.esrl.noaa.gov/psd/

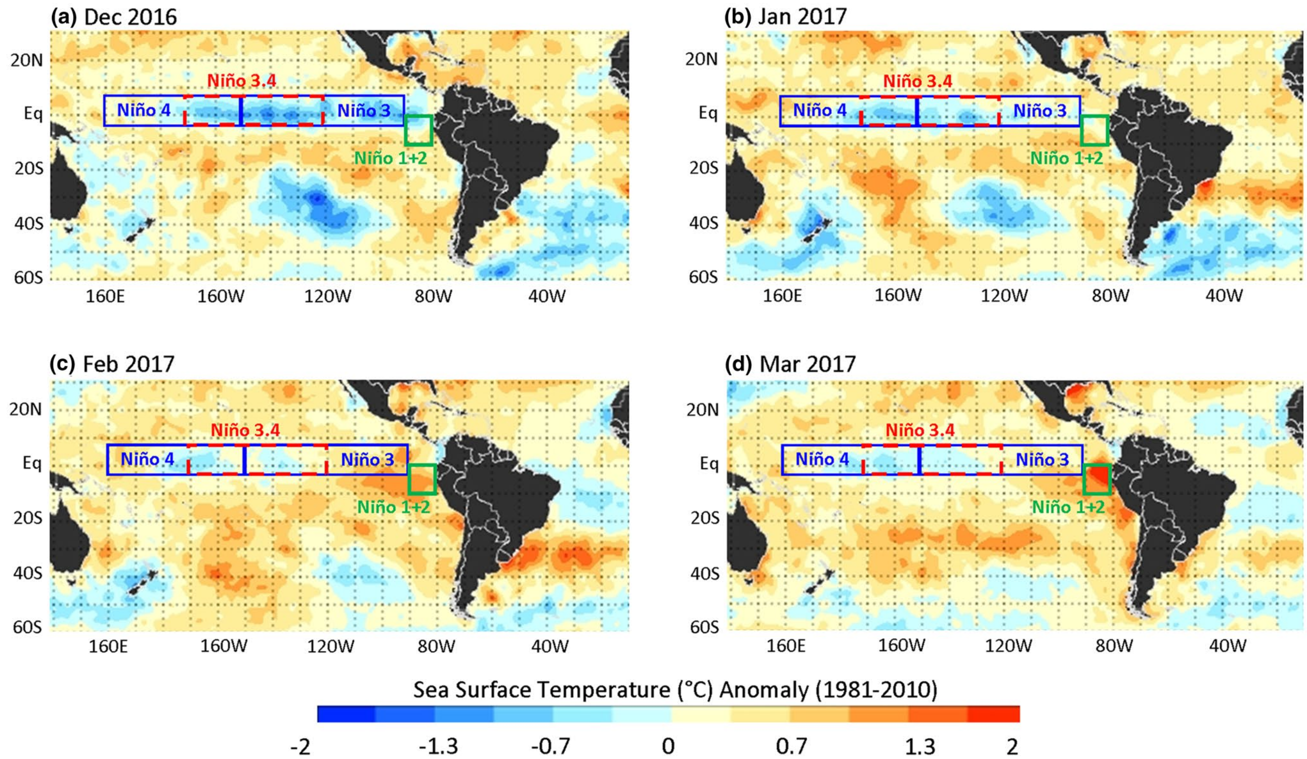

Fig. 8 Plots **a–d** show the evolution of the SST monthly anomaly in the equatorial Pacific between December 2016 and March 2017. We use HadISST1 data provided by the NOAA/OAR/ESRL PSD (http://www.esrl.noaa.gov/psd/)

negative SST anomalies started to become more intense in the equatorial Pacific, but remained restricted to region 3.4. At the same time, SST anomalies in the 1 + 2 region start to rise (Fig. 8b). Between February and March 2017, the SST anomaly was at its maximum with values 2.8 °C above the average in region 1 + 2 (Fig. 8c, d). Central Pacific SST anomalies were close to neutral values.

3.2.2 SOM analysis

The SOM maps corresponding to the anomalies of the geopotential (Z) and zonal wind anomaly (U) at 200, 500 and 850 hPa, as well as SST show 25 possibilities of synoptic settings during the austral summer (an overview of all SOM maps is provided in Figures S1–S7, Supporting information). The distribution of these 25 possibilities place contrasting situations in opposite sides of the SOM map (i.e., El Niño like patterns in the right side and La Niña in the left side) and a range of intermediate possibilities in between. Thus we find that strong El Niño events (i.e. 1982–1983, 1997–1998, 2009–2010, and 2015–2016) are mostly related with node 1E (Fig. 9) representing a pattern dominated by (1) a full-basin overwarming in the equatorial Pacific (Fig. S7) and (2) a strong positive 850 hPa zonal wind anomaly along the equatorial Pacific, characteristic of El Niño events (Fig. S6). In opposite, strong La Niña events (i.e. 1988–1989, 1998–1999, 1999–2000, 2007–2008 and 2010–2011) are related with nodes of column A, linked to different extensions of cooling in the equatorial Pacific (Fig. S7). Synoptic states related with neutral conditions are scattered in the center of the SOM grid (Fig. 9) and are related with variations in the strength and position of pressure centers over the continent, the south Pacific, and the south Atlantic (Fig S1, 2, 3). Weak-to-moderate ENSO extremes are also related to scattered synoptic states but exhibit a clear trend toward El Niño or La Niña sides of the SOM grid.

The temporal evolution and dominance (i.e. the number of days of pattern activity) of each generalized pattern during each austral summer since 1979 (considering 121 days between December to March) are represented in Fig. 9. We identify different pattern tracks depending on the ENSO phase (i.e. El Niño, La Niña, or neutral conditions). For strong El Niño and La Niña years, the path is restricted to few a patterns with very high dominance in each setting. For example, in the case of the strong El Niño in 1982–1983, 1997–1998 and 2015–2016, the dominance of the node 1E was of 61, 86, and 88 days, respectively. However, in the case of neutral and weak-moderate El Niño and La Niña years, the path is more diverse with less time at each node. For the 2016–2017 austral summer event, however, the path was very much restricted to the nodes in the central columns of the SOM map, and moves from nodes in the lower part of the grid (associated with cold SST in the equatorial Pacific), to nodes in the upper part (related with warmer SST in the 1 + 2 El Niño region than in the central Pacific). Upper-level pressure anomalies were negative to neutral at the beginning of the event and then evolve to very positive anomalies.

3.3 The 2017 coastal event in a larger context

Figure 10 represents the JFM averaged anomaly of El Niño 3.4 and 1 + 2 index values since 1870 to the present. The value corresponding to the 1 + 2 El Niño region (shaded in red Fig. 10 and indicated with a black arrow) during the 2016–2017 was only exceeded by years classified as El Niño events (i.e. 1878*, 1889, 1897, 1900, 1926, 1983*, 1987, 1997*, and 2016*; asterisks indicate strong El Niño events). The values corresponding to the summers following the decay of an El Niño event (Table 1) show that the 2017 JFM anomaly in the 1 + 2 El Niño region was significantly higher (0.94) than average (− 0.15). The situation in the 3.4 region is different as it presents a value (− 0.15) slightly above the average for 2017 but still negative and not significant. Regarding the OLR anomalies in El Niño 1 + 2 region since 1979 (Fig. 11), we observe that the negative anomaly during 2016–2017 austral summer only has been exceeded during the El Niño years in 1982–1983, 1997–1998, and 2009–2010.

Results of the SEA (Fig. 12) comparing the Niño SST indices (i.e. Niño 1 + 2 and 3.4) of several austral summers after El Niño events indicate that for the central Pacific (Niño 3.4 index; Fig. 11a) 2016–2017 SST anomaly values were not significantly far from the average for D (0) (i.e. index value − 0.47, p-value 0.098), J + 1 (i.e. index value − 0.44, p-value 0.177) and F + 1 (i.e. index value − 0.07, p-value 0.105). Since M + 1 (Mar 2017) the 3.4 SST anomaly was statistically significantly high but below of 1992–1993 austral summer. In the 1 + 2 SST index case, (Fig. 11b) results indicate statistically significant high values during the 2016–2017 austral summer for all the months of the period.

Figure 13 shows differences of the spatial distribution of the SST anomaly along the equatorial Pacific between the 2016–2017 austral summer and its counterparts in 1878–1879, 1983–1984 and 1998–1999. During the CEN-2017, the west-central Pacific (Niño 4 and 3.4 regions) in fact exhibited the lowest SST anomaly during December-March with the only negative values of the period. This cooling is coherent as such but still far from the negative values observed in 1878–1879, 1983–1984 and 1998–1999. The Pacific Niño 3 and 3.4 regions showed neutral to positive anomalies, which were again significantly higher in 2017 than in 1878–1879, 1983–1984 and 1998–1999 when the anomalies were clearly negatives. The east Pacific (Niño 1 + 2 region) displays by far the largest anomalies with maximum value of 2.1 °C during the CEN-2017, very different from the very negative values, which remained in this region for the other years.

4 Discussion and conclusions

During the 2016–2017 austral summer, intense rainfalls were recorded over large parts of Peru. The accumulated measured precipitation exceeded all summer values recorded since 1982, and led to catastrophic damage to housing and infrastructure, affecting more than 660,000 people, and leaving more than 100 deaths (INDECI 2017). Furthermore, the spatial and temporal synchronicity of these extraordinary rainfall values observed during the DJFM 2016–2017 in various and very diverse geographic settings across Peru can be described as unusual.

Our observations of the climatic background regarding the large-scale oceanic and atmospheric setting of this costal event agree with Garreaud (2018), who pointed to the role of extratropical climatic forcing. While it is true that between January and March 2017, positive anomalies of the sea surface height were detected along the Peruvian coast (these have been related to warming Kelvin waves activity impacting the north Peruvian coast), these waves contributed only partially to the SST warming in this region (ENFEN 2017a, b). In fact, time series (not shown) of subsurface sea temperatures and dynamic height of the sea surface obtained from the Tropical Atmosphere Ocean (TAO) array of buoys moored in the tropical Pacific do not provide clear evidence of Kelvin activity, suggesting they were not the primary mechanism associated with the strong coastal warming in 2017.

At the beginning of the 2016–2017 austral summer, the strongest rainfall totals were found over some areas of the Central Andes, in the Huánuco region. Even though seasonal rainfalls over the Peruvian Central Andes (and Peru in general) occur during the summer (IGP 2005; Sulca et al. 2016), the accumulated rainfall in January was the highest since 1982 over many of the Central Andes regions (i.e. San Martin, Huánuco, Pasto and Junín) as well as along the South coast (i.e. Arequipa) and over the Amazonian lowlands (i.e. south-west Loreto, Amazonas and Ucayali). According to our synoptic analysis, the long-lasting, upper-level anticyclone observed adjacent to the Chilean coast during January (Fig. 4a) led to an intensification of mid-upper level subtropical easterly winds (Fig. 4b) favoring a moisture flux from the Amazon basin and thus intense precipitation in the Central Andes. These observations agree with Garreaud (2000) and Sulca et al. (2016) who describe wet events over the Central Andes in relation with upper-level geopotential anomalies linked to the equatorward propagation of mid-latitude wave trains. This is also in line with Garreaud (1999, 2018), who found that the propagation of mid-latitude

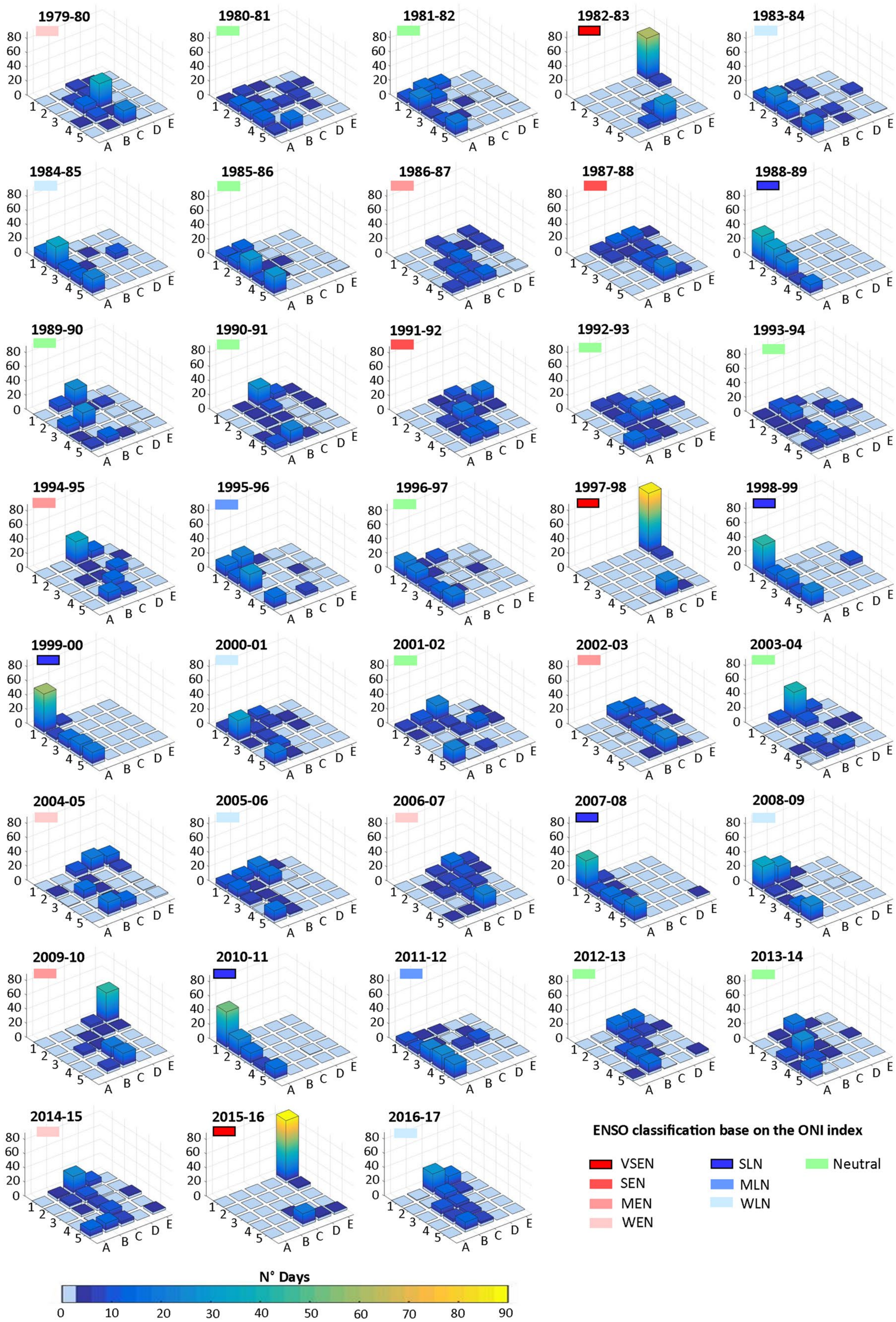
1979-80
1980-81
1981-82
1982-83
1983-84
1984-85
1985-86
1986-87
1987-88
1988-89
1989-90
1990-91
1991-92
1992-93
1993-94
1994-95
1995-96
1996-97
1997-98
1998-99
1999-00
2000-01
2001-02
2002-03
2003-04
2004-05
2005-06
2006-07
2007-08
2008-09
2009-10
2010-11
2011-12
2012-13
2013-14
2014-15
2015-16
2016-17
80
60
40
20
0
1
2
3
4
5
A
B
C
D
E
ENSO classification base on the ONI index
VSEN
SEN
MEN
WEN
SLN
MLN
WLN
Neutral
N° Days
0
10
20
30
40
50
60
70
80
90

◂**Fig. 9** Graphs showing the dominance of the synoptic patterns during the austral summers since 1979. The ONI classification of each austral summer is represented by the colored squares and the abbreviations correspond to: *VSEN* Very strong El Niño; *SEN* Strong El Niño; *MEN* Moderate El Niño; *WEN* Weak El Niño; *SLN* Strong La Niña; *MLN* Moderate La Niña; *WLN* Weak La Niña

Rossby wave trains drive rainfall variability on the Altiplano on intra-seasonal time scales.

During February and March 2017, the extreme rainfall values moved to the Peruvian north and central coast areas as well as to the Central Andes with cumulative March precipitation exceeding any other value for the same period since 1982 in many regions (Figs. 2, 3). For this period, OLR anomalies in the 1 + 2 El Niño region (Figs. 6, 11) were consistent with the exceptionally high values of SST in the region (Figs. 7, 8, 10, 13d), reaching levels that are normally indicative of the development of an El Niño event (Rasmusson and Carpenter 1982; Trenberth and Stepaniak 2001). Furthermore, Fig. 4b shows that the upper-level subtropical easterlies were reinforced, which, according to Garreaud (2018), could have modified the subtropical circulation in the lower troposphere and in turn may have directly affected SST in the eastern equatorial Pacific (Fig. 5). In fact, the continued strength of the easterly trades in the equatorial band is supported by the low-level equatorward flow along the Pacific coast of South America, generated by descent when the subtropical westerlies meet the Andes (Rodwell and Hoskins 2001). If the subtropical westerlies are weak or reversed, this equatorward flow does not provide the mass continuity to the SE trade winds, thus hampering the upwelling along the coast and leading to surface warming in the eastern Pacific.

We also point to the potential role of SST in the South Atlantic and the SACZ during the CEN-2017 event. As observed in Fig. 8, an intense positive anomaly is observed in the South Atlantic centered at 40°S, 40°W, coincident with a SST anomaly in the equatorial Pacific, OLR negative anomaly over the SACZ (Fig. 6), and heavy rainfalls over the Peruvian central Andes (Figs. 2, 3). This situation is coherent with findings of Rodrigues-Chaves and Nobre (2004) and Carvalho et al. (2004), who stated that positive correlation exists between SST over the South Atlantic (from the 40°S–0°) and the SACZ. Furthermore, our observations are in line with Lavado-Casimiro et al. (2013) who found that higher values in the southern tropical Atlantic (0–20°S, 30°W–10°E) than in the north tropical Atlantic (5–20°N, 60–30°W) favor precipitation in the Peruvian Amazon-Andes. On the other hand, the intensification of the convective activity in the SACZ in January (Fig. 6b) could be related to the rainfall in the Central Andes by controlling the position of the Bolivian High (Lenters and Cook 1999).

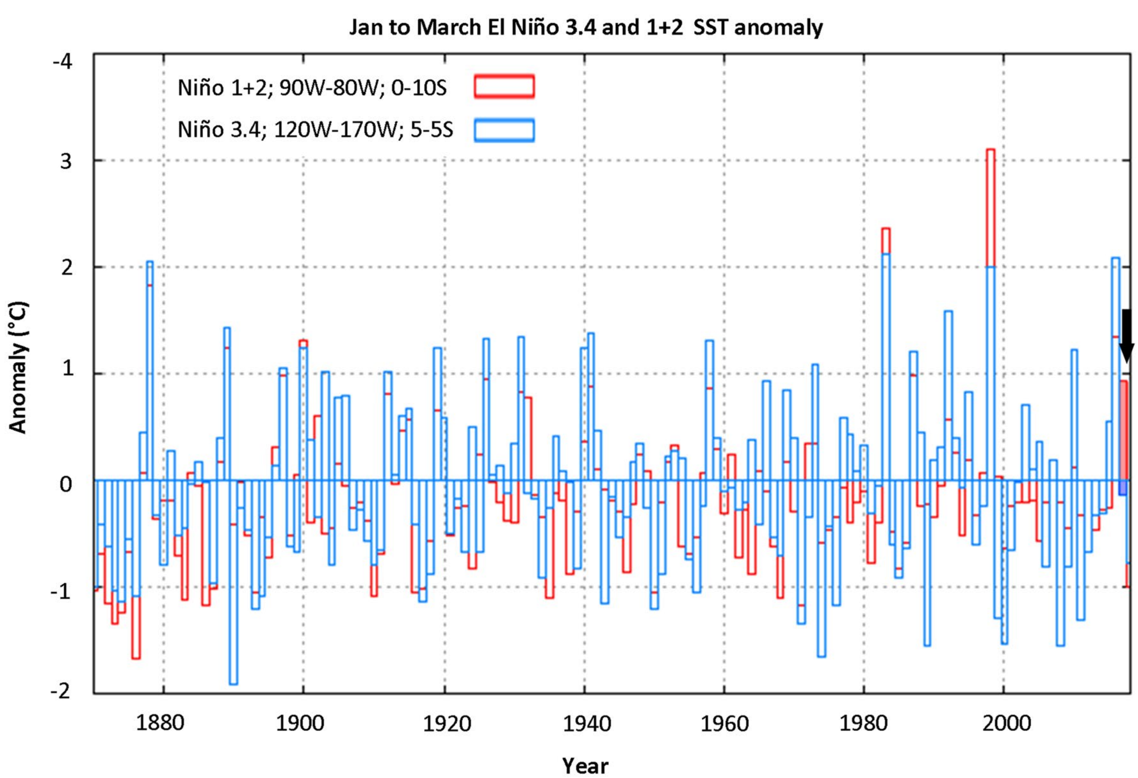

Fig. 10 Niño 3.4 and 1 + 2 indices since 1870. The black arrow indicates the year 2017

Table 1 JFM SST anomalies in the 1+2 and 3.4 El Niño regions corresponding to years following the decay of an El Niño event since 1870 and indicating either neutral or weak La Niña conditions

	JFM El Niño 1+2 SST anomaly	JFM El Niño 3.4 SST anomaly
1879	−0.36*	−0.32*
1890	−0.42*	−1.92*
1898	−0.51*	−0.6*
1904	−0.44*	−0.8*
1927	−0.013*	0.05
1967	−0.63*	−0.53*
1984	−0.49*	−0.6*
1999	0.04*	−1.29*
2017	0.94*	−0.15
1870–2017 average	−0.15	−0.073

The 2017 year was significantly above the average in the 1+2 El Niño region, indicating a clear El Niño situation. The situation in the 3.4 region reflects temperatures slightly under the average but they are not significant. Note that the considered cases are those where the SST values in the Niño region decay toward zero during the remaining months of year+1 of the El Niño event. Some Niño's do not follow that decay mode pattern, and so are not included here. Statistical significance computed using a t-test for one-sided samples at a significance level of 0.05 (below)

*Significant values

Finally, the southward shift of the SACZ observed in February (Fig. 6c) could be related with the enhanced tropical convection over the central and eastern Pacific (Nogues-Paegle and Mo 1997).

Striking rainfall totals and high rank percentiles in the northern interior lowlands of Piura and Lambayeque as well as in southern region up to La Libertad during March 2017 are consistent with studies stating that inter-annual rainfall variability in these regions cannot be explained by El Niño activity alone (Lagos et al. 2008; Lavado-Casimiro and Espinoza 2014; Rau et al. 2017). For instance, Rau et al. (2017) state that inter-annual variations of rainfall do not necessarily correspond to strong El Niño years, and that an important part of rainfall variability in the region may correspond to local convective events associated with coastal warm oceanic conditions related mainly to Kelvin waves and the Madden and Julian Oscillation (MJO) (Bourrel et al. 2015). By contrast, inter-annual rainfall variability in the northern highlands of Cajamarca was not clearly related with SST in the east Pacific, but negatively correlated with SST in the central Pacific (Bourrel et al. 2015; Rau et al. 2017). This is consistent with the negative anomalies that we observe in the west-central Pacific (Niño 4 and 3.4 regions in Fig. 8). Regarding rainfall activity in the Peruvian Amazonian lowlands, rainfall totals reached their long-term maxima mostly during January–February 2017 as well. We hypothesize that this anomaly can be related with the positive SST

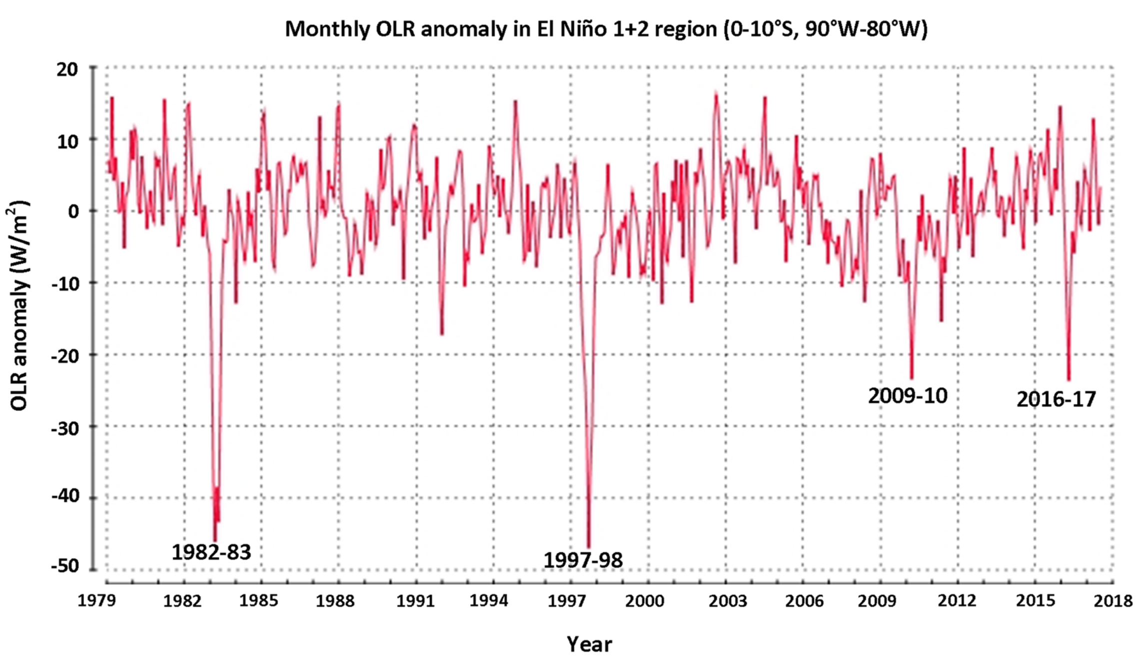

Fig. 11 Time series of OLR anomaly in El Niño 1+2 region since 1979

anomalies in the South Tropical Atlantic observed in Fig. 8c. This hypothesis is consistent with Espinoza et al. (2009) or Lavado-Casimiro et al. (2013) who concluded that intense rainfalls over Peru are likely related with the positive SST anomalies observed in the South Tropical Atlantic. Yet, further research is needed to understand the role of the tropical Atlantic during the CEN-2017 event.

The warming in the equatorial Pacific was not a full basin event and the SOI index, with values close to zero (not shown) indicates that the CEN-2017 event was not a coupled ocean–atmosphere phenomenon. As such, it differs from a typical El Niño and defines it like an ocean-coastal event (Takahashi and Martinez 2017). Considering the SST values in the eastern Pacific, this 2016–2017 summer also differs from its counterparts after El Niño events since 1870 (Fig. 10, 11, 12 and 13). Differences with previous years are also noticed in the transition between synoptic states throughout the summer (Fig. 9). Even if the synoptic states related with the 2016–2017 austral summer are commonly linked to the large-scale summer dynamic over South America and are not exclusive of the 2016–2017 summer, what is different this time is the low dispersion and relatively low number of synoptic states compare with previous years (except for the strong El Niño and La Niña years). Thus, dominance of these synoptic states was higher, favoring the climatic processes that trigger the overwarming in the equatorial Pacific. Consequently, the usual precipitation pattern after a strong El Niño event—with slightly above-normal rainfalls in the south of Peru and nearly normal to dry conditions in the north—was altered after the end of the 2015–2016 El Niño, as it did not result in the usual cooling of the central equatorial Pacific (Lavado-Casimiro and Espinoza 2014).

We conclude that the coexistent SST anomalies in the equatorial Pacific (and presumably also in the Tropical Atlantic) have clearly favoured the development of the extreme "Coastal El Niño" event and concomitant high magnitude of precipitation over Peru in DJFM 2016–2017. The approach shown in this paper, together with its interpretation within a climatic context, demonstrates that the DJFM 2016–2017 rainfall pattern over Peru was highly anomalous, both in terms of its magnitude and timing after a strong El Niño event. The rather severe consequences and important death tolls cannot be explained by the anomalous weather phenomenon only, but are also due to the absence of El Niño early warnings, which in turn were largely the result of the abrupt and unexpected warming above the average in the Niño region 1 + 2. This suggests that disaster management strategies in Peru should maintain the same level of vigilance across time, regardless of the ENSO phase, taking into account the whole variability of South American summers.

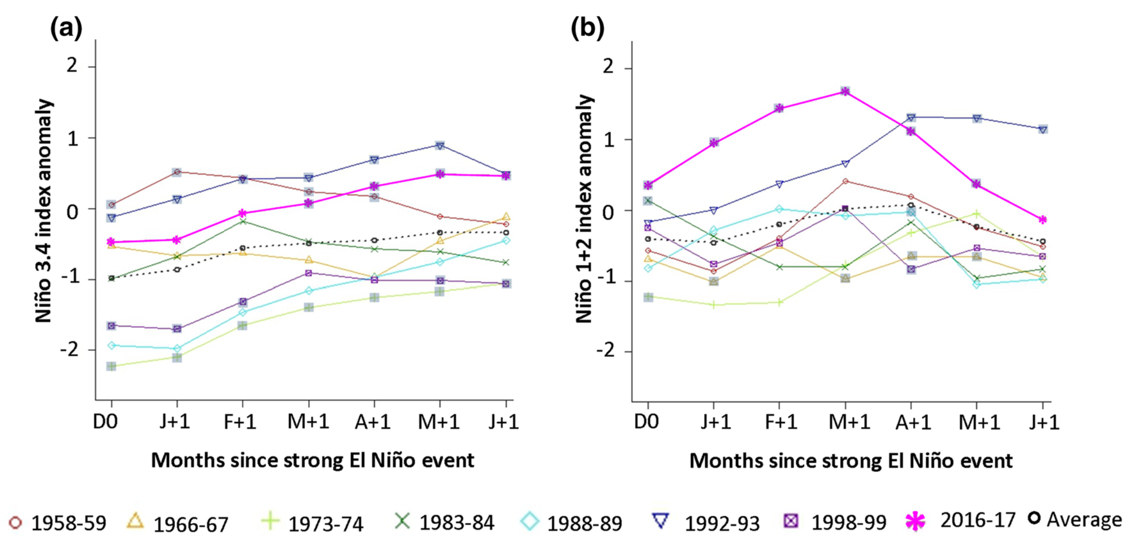

Fig. 12 Superposed epoch analysis for the anomalies of the 3.4 (**a**) and 1 + 2 (**b**) El Niño indices during the year after strong El Niño events since 1951. Following the nomenclature system of Rasmusson and Carpenter (1982), analysis covers the months of December after an El Niño event (D0) to June of the following year (J + 1) and they are centered in March 2017 (M + 1). Shades years are statically significant at 0.05 level

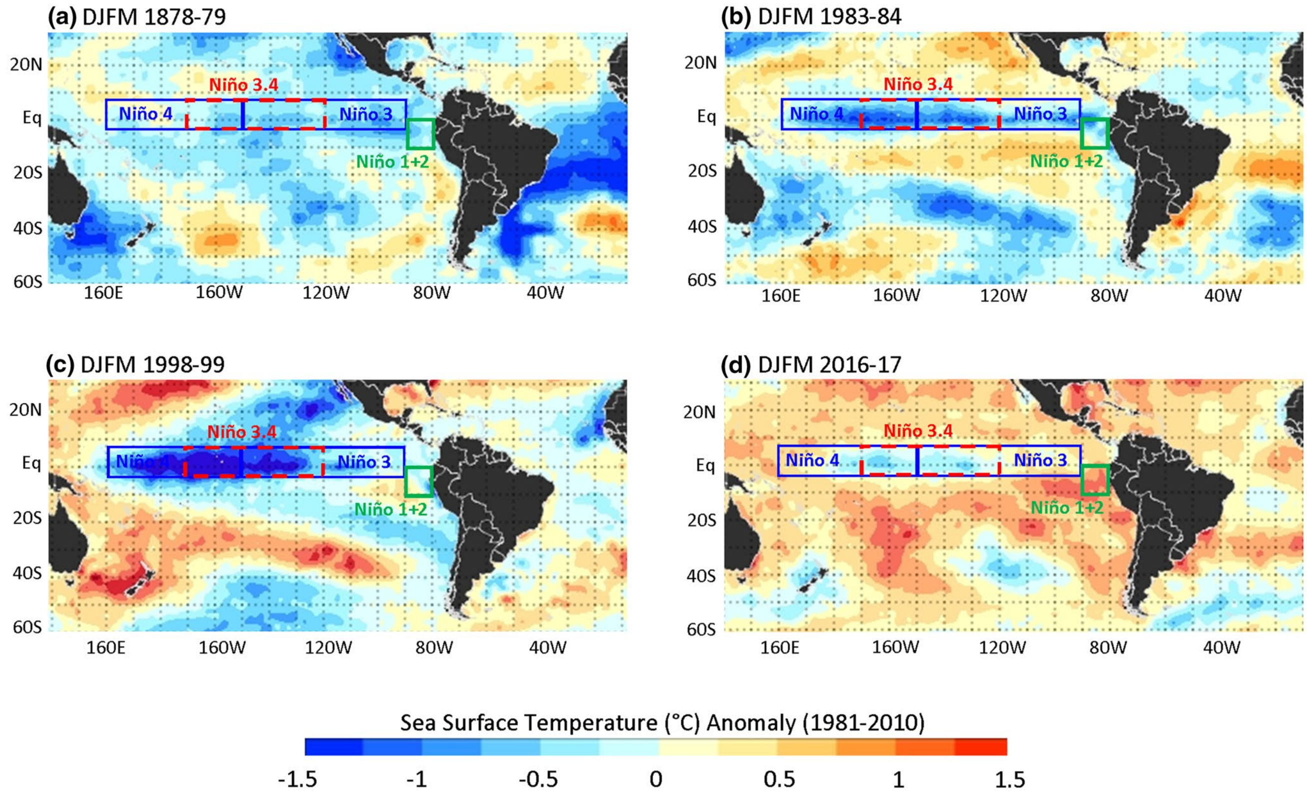

Fig. 13 Sea surface temperature (SST) anomaly maps for December to March for the first austral summer after the strong El Niño events in 1877–1878, 1982–1983, 1997–1998 and 2015–2016. We use HadISST1 data provided by the NOAA/OAR/ESRL PSD (http://www.esrl.noaa.gov/psd/)

Acknowledgements The authors wish to thank Dr. Rene Garreaud and the two anonymous reviewers whose comments and suggestions considerably helped to improve the manuscript.

References

Ashok K, Behera SK, Rao SA, Weng H, Yamagata T (2007) El Niño Modoki and its possible teleconnections. J Geophys Res 112:C11007. https://doi.org/10.1029/2006JC003798

Bourrel L, Rau P, Dewitte B, Labat D, Lavado W, Coutaud A, Vera A, Alvarado A, Ordoñez J (2015) Low-frequencymodulation and trend of the relationship between ENSO and precipitation along the northern to centre Peruvian Pacific coast. Hydrol Process 29(6):1252–1266

Capotondi A et al (2015) Understanding ENSO diversity. Bull Am Meteorol Soc 96:921–938

Carvalho LMV, Jones C, Liebmann B (2004) The South Atlantic Convergence Zone: intensity, form, persistence, and relationships with intraseasonal to interannual activity and extreme rainfall. J Clim 17: 88–108. https://doi.org/10.1175/1520-0442(2004)017%3C0088:TSACZI%3E2.0.CO;2

Cassano EN, Lynch AH, Cassano JJ, Koslow MR (2006a) Classification of synoptic patterns in the western Arctic associated with extreme events at Barrow, Alaska, USA. Clim Res 30(2):83–97

Cassano JJ, Uotila O, Lynch A (2006b) Changes in synoptic weather patterns in the polar regions in the 20th and 21st centuries, part 1: Arctic. Int J Climatol 26:1027–1049

Cassano JJ, Uotilla P, Lynch AH, Cassano EN (2007) Predicted changes in synoptic forcing of net precipitation in large Arctic river basins during the 21st century. J Geophys Res. https://doi.org/10.1029/2006JG000332

CPC (2018a) ENSO Diagnostic Discussion Archive. http://www.cpc.ncep.noaa.gov/products/expert_assessment/ENSO_DD_archive.shtml. Accessed 25 May 2018

CPC (2018b) http://www.cpc.ncep.noaa.gov/products/analysis_monitoring/ensostuff/ONI_v5.php. Accessed 25 May 2018

Dee DP et al (2011) The ERA-Interim reanalysis: configuration and performance of the data assimilation system. Q J R Meteor Soc 137:553–597

Dommenget D, Bayr T, Frauen C (2013) Analysis of the non-linearity in the pattern and time evolution of El Niño Southern Oscillation. Clim Dyn 40:2825–2847. https://doi.org/10.1007/s00382-012-1475-0

ECMWF (2016) ERA-Interim daily data. http://apps.ecmwf.int/datasets/data/interim-full-daily/levtype=sfc/. Accessed 10 Jan 2016

ENFEN (2017a) Comunicados oficiales. https://www.dhn.mil.pe/comunicado_oficial_enfen. Accessed 13 Sep 2017

ENFEN (2017b) Informe Técnico Extraordinario No 001-2017/ENFEN EL NIÑO COSTERO 2017. Resumen ejecutivo. http://www.imarpe.pe/imarpe/archivos/informes/imarpe_inftco_informe__tecnico_extraordinario_001_2017.pdf. Accessed 18 Sep 2018

Espinoza JC, Ronchail J, Guyot JL, Cochonneau G, Naziano F, Lavado W, Oliveira ED, Pombosa R, Vauchel P (2009) Spatio-temporal rainfall variability in the Amazon basin countries (Brazil, Peru, Bolivia, Colombia, and Ecuador). Int J Clim 29:1574–1594

Espinoza JC, Lengaigne M, Ronchail J, Anicot S (2012) Large-scale circulation patterns and related rainfall in the Amazon Basin: a neuronal networks approach. Clim Dyn 38(1–2):121–140. https://doi.org/10.1007/s00382-011-1010-8

Espinoza JC, Ronchail J, Lengaigne M, Quispe N, Silva Y, Bettolli M, Avalos G, Llacza A (2013) Revisiting wintertime cold air intrusions at the east of the Andes: propagating features from subtropical Argentina to Peruvian Amazon and relationship with large-scale circulation patterns. Clim Dyn 41(7–8):1983–2002. https://doi.org/10.1007/s00382-012-1639-y

Few R (2007) Health and climate change hazards: framing social research on vulnerability, response and adaptation. Glob Environ Change 17:281–295

Garreaud RD (1999) Multiscale analysis of the summertime precipitation over the central Andes. Mon Weather Rev 127:901–921. https://doi.org/10.1175/1520-0493(1999)127,0901:MAOTSP.2.0.CO;2

Garreaud RD (2000) Intraseasonal variability of moisture and rainfall over the South American Altiplano. Mon Weather Rev 128:3337–3346

Garreaud RD (2018) A plausible atmospheric trigger for the 2017 coastal El Niño. Int J Climatol 38(Suppl. 1):e1296 e1302

Garreaud RD, Vuille M, Compagnucci R, Marengo J (2009) Present-day South American climate. Paleogeogr Palaeoclimatol Palaeoecol 281:180–195

Hales S, Edwards S, Kovats RS (2003) Impacts on health of climate extremes. In: McMichael A, Campbell-Lendrum D, Corvala´n C, Ebi K, Githeko A, Scheraga J, Woodward A (eds) Climate change and human health: risks and response. World Health Organization, Geneva, pp 79–102

Haynes W (2013) Student's t-test. In: Dubitzky W, Wolkenhauer O, Cho KH, Yokota H (eds) Encyclopedia of systems biology. Springer, New York. https://doi.org/10.1007/978-1-4419-9863-7

Hewitson B, Crane R (2002) Self-organizing maps: applications to synoptic climatology. Clim Res 22:13–26

Hong Y, Hsu K, Sorooshian S, Gao X (2005) Self-organizing nonlinear output (SONO): a neural network suitable for cloud patch-based rainfall estimation at small scales. Water Resour Res. https://doi.org/10.1029/2004WR003142

Huffman G (2015) GPM IMERG final precipitation L3 1 month 0.1 degree × 0.1 degree V04, Greenbelt, MD, Goddard Earth Sciences Data and Information Services Center (GES DISC). Accessed 15 Feb 2018. https://doi.org/10.5067/GPM/IMERG/3B-MONTH/04

Huffman GJ, Bolvin DT, Braithwaite D, Hsu K, Joyce R, Kidd C, Nelkin EJ, Sorooshian S, Tan J, Xie P (2017) Algorithm theoretical basis document (ATBD) version 5.1 NASA global precipitation measurement (GPM) integrated multi-satellite retrievals for GPM (IMERG). https://pmm.nasa.gov/sites/default/files/document_files/IMERG_ATBD_V5.1.pdf. Accessed 15 Feb 2018

IGP (2005) Atlas climatológico de precipitaciones y temperaturas en la Cuenca del Río Mantaro. CONAM, Lima, Perú. http://www.met.igp.gob.pe/publicaciones/2000_2007/Atlas_Climatico.pdf

INDECI (2017) Resúmen ejecutivo—Temporada de lluvias Diciembre 2016—Marzo 2017. http://www.indeci.gob.pe/objetos/alerta/MjYxNg==//20170330165025.pdf

Johnson NC, Feldstein SB, Tremblay B (2008) The continuum of Northern Hemisphere teleconnection patterns and a description of the NAO shift with the use of self-organizing maps. J Clim 21:6354–6371

Kalnay E, Kanamitsu M, Kistler R, Collins W, Deaven D, Gandin L, Iredell M, Saha S, White G, Woollen J (1996) The NCEP/NCAR 40-year reanalysis project. Bull Am Meteorol Soc 77:437–471

Kao HY, Yu JY (2009) Contrasting Eastern-Pacific and Central-Pacific types of ENSO. J Clim 22:615–632

Kohonen T (2001) Self-organizing maps. Springer, New York

Kug JS, Jin FF, An SI (2009) Two types of El Niño events: cold tongue El Niño and warm pool El Niño. J Clim 22:1499–1515

L'Heureux M et al (2017) Observing and predicting the 2015/16 El Niño. Bull Amer Meteor Soc. https://doi.org/10.1175/BAMS-D-16-0009.1

Lagos P, Silva Y, Nickl E, Mosquera K (2008) El Niño—related precipitation variability in Peru. Adv Geosci 14:231–237

Larkin NK, Harrison DE (2005) On the definition of El Niño and associated seasonal average US weather anomalies. Geophys Res Lett 32:L13705. https://doi.org/10.1029/2005GL022738

Lavado-Casimiro W, Espinoza J (2014) Impactos de El Niño y La Niña en las lluvias del Perú (1965–2007). Rev Bras Meteorol 29:171–182

Lavado-Casimiro WS, Labat D, Ronchail J, Espinoza JC, Guyot JL (2013) Trends in rainfall and temperature in the Peruvian Amazon–Andes basin over the last 40 years (1965–2007). Hydrol Process. https://doi.org/10.1002/hyp.9418

Lenters JD, Cook KH (1997) On the origin of the Bolivian High and related circulation features of the South American climate. J Atmos Sci 54:656–677

Lenters JD, Cook KH (1999) Summertime precipitation variability over South America: role of the large-scale circulation. Mon Weather Rev 127:409–431

Lynch A, Uotila P, Cassano JJ (2006) Changes in synoptic weather patterns in the polar regions in the twentieth and twenty-first centuries (Part 2). Antarctic. Int J Climatol 26:1181–1199

Morata A, Martin ML, Luna MY, Valero F (2006) Self-similarity patterns of precipitation in the Iberian Peninsula. Theor Appl Climatol 85:41–59

NCAR (2014) Outgoing longwave radiation (OLR): AVHRR. The climate data guide. Boulder, CO. https://climatedataguide.ucar.edu/climate-data/outgoing-longwave-radiation-olr-avhrr. Accessed 15 Jun 2018

NOAA (2017) ENSO diagnostic discussion (climate prediction center, Nov–Dec 2017). http://origin.cpc.ncep.noaa.gov/products/analysis_monitoring/enso_disc_jun2014/. Accessed 25 Feb 2018

Nogues-Paegle J, Mo KC (1997) Alternating wet and dry conditions over South America during summer. Mon Weather Rev 125:279–291

Paccini L, Espinoza JC, Ronchail J, Segura H (2017) Intraseasonal rainfall variability in the Amazon basin related to large-scale circulation patterns: a focus on western Amazon-Andes transition region. Int J Clim 38(5):2386–2399

PAHO (2017) Emergencia por impacto del Fenómeno "El Niño Costero"—Perú, 2017. Pan American Health Organization, Washington, DC

Rasmusson EM, Carpenter TH (1982) Variations in tropical sea surface temperature and surface wind fields associated with the Southern oscillation/El Niño. Mon Weather Rev 110:354–384

Rau P et al (2017) Regionalization of rainfall over the Peruvian Pacific slope and coast. Int J Clim. https://doi.org/10.1002/joc.4693

Rayner NA, Parker DE, Horton EB, Folland CK, Alexander LV, Rowell DP, Kent EC, Kaplan A (2003) Global analyses of sea surface temperature, sea ice, and night marine air temperature since the late nineteenth century. J Geophys Res 108(D14):4407. https://doi.org/10.1029/2002JD002670

Reusch DB, Alley RB, Hewitson BC (2005a) Relative performance of self-organizing maps and principal component analysis in pattern extraction from synthetic climatological data. Polar Geogr 29:227–251

Reusch DB, Hewitson BC, Alley RB (2005b) Towards ice core-based synoptic reconstructions of West Antarctic climate with artificial neural networks. Int J Climatol 25:581–610

Reusch DB, Alley RB, Hewitson BC (2007) North Atlantic climate variability from a self-organizing map perspective. J Geophys Res. https://doi.org/10.1029/2006JD007460

Rodrigues-Chaves R, Nobre P (2004) Interactions between sea surface temperature over the South Atlantic Ocean and the South Atlantic Convergence Zone. Geophys Res Lett 31:L03204. https://doi.org/10.1029/2003GL018647

Rodriguez-Morata C, Ballesteros-Canovas JA, Rohrer M, Espinoza JC, Beniston M, Stoffel M (2018) Linking atmospheric patterns with hydro-geomorphic disasters in Peru. Int J Climatol. https://doi.org/10.1002/joc.5507

Rodwell MJ, Hoskins BJ (2001) Subtropical anticyclones and summer monsoons. J Clim 14:3192–3211

Sanabria J, Bourrel L, Dewitte B, Frappart F, Rau P, Olimpio S, Labat D (2018) Rainfall along the coast of Peru during strong El Niño events. J Int Climatol. https://doi.org/10.1002/joc.5292

Schneider U, Becker A, Finger P, Meyer-Christoffer A, Ziese M (2015) GPCC monitoring product: near real-time monthly land-surface precipitation from rain-gauges based on SYNOP and CLIMAT data. Deutscher Wetterdienst. https://doi.org/10.5676/DWD_GPCC/MP_M_V5_100

Schuenemann KC, Cassano JJ, Finnis J (2009) Synoptic forcing of precipitation over Greenland: climatology for 1961–99. J Hydrometeorol 10:60–78

Schwarb M, Acuña D, Konzelmann T, Rohrer M, Salzmann N, Serpa Lopez B, Silvestre E (2011) A data portal for regional climatic trend analysis in a Peruvian High Andes region. Adv Sci Res 6:219–226. https://doi.org/10.5194/asr-6-219-2011

Seefeldt MW, Cassano JJ (2008) An analysis of low-level jets in the Greater Ross Ice Shelf region based on numerical simulations. Mon Weather Rev 136:4188–4205

Skific N, Francis JA, Cassano JJ (2009a) Attribution of projected changes in atmospheric moisture transport in the Arctic: a self-organizing map perspective. J Clim 22:4135–4153

Skific N, Francis JA, Cassano JJ (2009b) Attribution of seasonal and regional changes in Arctic moisture convergence. J Clim 22:5115–5134

Sulca J, Vuille M, Silva Y, Takahashi K (2016) Teleconnections between the Peruvian central Andes and northeast Brazil during extreme rainfall events in austral summer. J Hydrometeorol 17:499–515

Sulca J, Takahashi K, Espinoza JC, Vuille M, Lavado-Casimiro W (2017) Impacts of different ENSO flavors and tropical Pacific convection variability (ITCZ, SPCZ) on austral summer rainfall in South America, with a focus on Peru. Int J Climatol 38:420–435. https://doi.org/10.1002/joc.5185

Takahashi K, Martínez AG (2017) The very strong El Niño in 1925 in the far-eastern Pacific. Clim Dyn. https://doi.org/10.1007/s00382-017-3702-1

Takahashi K, Montecinos A, Goubanova K, Dewitte B (2011) ENSO regimes: reinterpreting the canonical and Modoki El Niño. Geophys Res Lett 38:L10704. https://doi.org/10.1029/2011GL047364

Trenberth K (2016) The climate data guide: Nino SST indices (Nino 1 + 2, 3, 3.4, 4; ONI and TNI). https://climatedataguide.ucar.edu/climate-data/nino-sst-indices-nino-12-3-34-4-oni-and-tni. Accessed 22 Jun 2018

Trenberth K, Stepaniak DP (2001) Indices of El Niño evolution. J Clim 14:1697–1701

Uotila P, Lynch AH, Cassano JJ, Cullather RI (2007) Changes in Antarctic net precipitation in the 21st century based on Intergovernmental Panel on Climate Change (IPCC) model scenarios. J Geophys Res. https://doi.org/10.1029/2006JD007482

Waring S, Brown B (2005) The threat of communicable diseases following natural disasters: a public health response. Disaster Manag Response 3:41–47

Wise E, Dannenberg M (2014) Persistence of pressure patterns over North America and the North Pacific since AD 1500. Nat Commun. https://doi.org/10.1038/ncomms5912

Yeh SW, Kug JS, Dewitte B, Kwon MH, Kirtman B, Jin FF (2009) El Niño in a changing climate. Nature. https://doi.org/10.1038/nature08316

Yu JY, Kao HY, Lee T, Kim ST (2011) Subsurface ocean temperature indices for central-Pacific and eastern-Pacific types of El Niño and La Niña events. Theor Appl Climatol. https://doi.org/10.1007/s00704-010-0307-6

Zhang R, Wang Y, Liu W et al (2006) Cloud classification based on self-organizing feature map and probabilistic neural network. In: Proceedings of the 6th World Congress on Intelligent Control and Automation, 21–23 June 2006, Dalian, China, pp 41–45